



Royal Netherlands Institute for Sea Research

This is a postprint of:

Stocchi, P.; Antonioli, F.; Montagna, P.; Pepe, F.; Lo Presti, V.; Caruso, A.; Corradino, M.; Dardanelli, G.; Renda, P.; Frank, N.; Douville, E.; Thil, F.; de Boer, B.; Ruggieri, R.; Sciortino, R. & Pierre, C. (2017). A stalactite record of four relative sea-level highstands during the Middle Pleistocene Transition. *Quaternary Science Reviews*, 173, 92-100

Published version: <https://dx.doi.org/10.1016/j.quascirev.2017.08.008>

Link NIOZ Repository: [www.vliz.be/nl/imis?module=ref&refid=288522](http://www.vliz.be/nl/imis?module=ref&refid=288522)

[Article begins on next page]

The NIOZ Repository gives free access to the digital collection of the work of the Royal Netherlands Institute for Sea Research. This archive is managed according to the principles of the [Open Access Movement](#), and the [Open Archive Initiative](#). Each publication should be cited to its original source - please use the reference as presented.

When using parts of, or whole publications in your own work, permission from the author(s) or copyright holder(s) is always needed.

1 **A stalactite record of four relative sea-level highstands during the Middle Pleistocene**  
2 **Transition**

3  
4 Paolo Stocchi<sup>1,\*</sup>, Fabrizio Antonioli<sup>2</sup>, Paolo Montagna<sup>3</sup>, Fabrizio Pepe<sup>4</sup>, Valeria Lo Presti<sup>2</sup>, Antonio  
5 Caruso<sup>4</sup>, Marta Corradino<sup>4</sup>, Gino Dardanelli<sup>5</sup>, Pietro Renda<sup>4</sup>, Norbert Frank<sup>6</sup>, Eric Douville<sup>7</sup>, François  
6 Thil<sup>7</sup>, Bas de Boer<sup>8</sup>, Rosario Ruggieri<sup>9,10</sup>, Rosanna Sciortino<sup>5</sup> and Catherine Pierre<sup>11</sup>

7  
8 <sup>1</sup>*NIOZ Royal Netherlands Institute for Sea Research, Department of Coastal Systems, and Utrecht*  
9 *University, Landsdiep 4, 1797 TA, Den Hoorn, Texel, the Netherlands*

10 <sup>2</sup>*ENEA National Agency for New Technologies, Energy and Environment, Via Anguillarese 301,*  
11 *00060, S. Maria di Galeria, Rome, Italy*

12 <sup>3</sup>*ISMAR-CNR, Via Gobetti 101, 40129 Bologna, Italy*

13 <sup>4</sup>*Dipartimento di Scienze della Terra e del Mare, Via Archirafi, 22, Università di Palermo, Palermo,*  
14 *Italy*

15 <sup>5</sup>*Dipartimento di Ingegneria Civile, Ambientale, dei Materiali (DICAM), Università di Palermo, Viale delle*  
16 *Scienze, Ed. 8, 90128 Palermo, Italy*

17 <sup>6</sup>*Universität Heidelberg, Im Neuenheimer Feld 229, 69120 Heidelberg, Germany*

18 <sup>7</sup>*LSCE/IPSL, UMR 8212 CNRS-CEA-UVSQ, 91198, Gif-sur-Yvette, France*

19 <sup>8</sup>*IMAU, Utrecht University, Utrecht, The Netherlands*

20 <sup>9</sup>*CIRS Centro Ibleo di Ricerche Speleo-Idrogeologiche, Via Torrenuova 87, 97100, Ragusa, Italy*

21 <sup>10</sup>*University of Nova Gorica, SI-5000 Nova Gorica, Slovenia*

22 <sup>11</sup>*LOCEAN, Jussieu, Paris Cedex, France*

23  
24 *\*Corresponding author: Paolo.Stocchi@nioz.nl*

25

26

27 **Abstract**

28 Ice-sheet and sea-level fluctuations during the Early and Middle Pleistocene are as yet poorly  
29 understood. A stalactite from a karst cave in North West Sicily (Italy) provides the first evidence of  
30 four marine inundations that correspond to relative sea-level (RSL) highstands at the time of the  
31 Middle Pleistocene Transition. The speleothem is located ~ 97 m above mean sea level (msl) as result  
32 of Quaternary uplift. Its section reveals three marine hiatuses and a coral overgrowth that fixes the age  
33 of the fourth and final marine ingression at  $1.124 \pm 0.2$  million years ago, thus making this speleothem  
34 the oldest stalactite with marine hiatuses ever studied to date. Scleractinian coral species witness light-  
35 limited conditions and water depth of 20-50 m. Integrating the coral-constrained depth with the  
36 geologically constrained uplift rate and an ensemble of RSL scenarios, we find that the age of the last  
37 marine ingression most likely coincides with Marine Isotope Stage 35 on the basis of a probabilistic  
38 assessment. Our findings are consistent with a significant Antarctic ice-sheet retreat.

39

40 Keywords: Interglacial(s); Pleistocene; Sea Level changes; Paleogeography; Western Europe;  
41 Speleothems; Corals, Stable isotopes; U-Th dating;  $^{87}\text{Sr}/^{86}\text{Sr}$  ages, Geomorphology, coastal  
42

43

44 **1. Introduction**

45 Changes in solar radiation due to orbital forcing and variations in the concentrations of atmospheric  
46 greenhouse gases led to a succession of glacial and interglacial periods during the Pleistocene (Bintanja  
47 et al., 2005; De Boer et al., 2013; Rohling et al., 2014). Large fluctuations in ice volumes on both  
48 hemispheres resulted in significant sea-level changes that can be inferred from proxy records such as  
49 benthic and planktonic foraminiferal  $\delta^{18}\text{O}$  from deep-sea sediment cores (Rohling et al., 2014; Lisiecki  
50 and Raymo, 2004; Grant et al., 2014). However,  $\delta^{18}\text{O}$  time series lack direct age control and require  
51 numerical iteration to decouple the convolved deep-water temperature and global ice mass signal  
52 (Bintanja et al., 2005; De Boer et al., 2014). Relative sea-level (RSL) changes can be permanently

53 recorded by coastal geomorphological markers that are linked to coastal uplift (Ferranti et al., 2006;  
54 Antonioli et al., 2015). A common approach in constraining Pleistocene ice-sheet fluctuations is to date  
55 RSL markers such as shallow karst cave speleothems and measure their elevations with respect to  
56 modern mean sea level. The subaerial growth of speleothems inside caves that are connected to the sea  
57 is interrupted during marine floodings. Successive marine inundations appear as series of concentric  
58 hiatuses within speleothem sections and can be converted into RSL changes (Dutton et al., 2009;  
59 Richards et al., 1994). While paleo sea-level markers such as fossil beaches from the Pliocene have  
60 been identified worldwide (Rovere et al., 2014), speleothems that can be used as reliable RSL  
61 indicators that are older than 1 million years are extremely rare because of cliff retreat due to coastal  
62 erosion and active tectonics (Breitenbach et al., 2005; Artyushkov, 2012).

63 In this work we reconstruct the conditions and the chronology of the events that led to the occurrence  
64 and preservation of four marine ingressions that are recorded by a stalactite that is located inside the  
65 uplifted Rumena karst cave (RKC) in Custonaci, North West Sicily (NWS; Fig. 1, 2). The descriptive  
66 work of Ruggieri and De Waele (2014) provides information on the RKC morphology as well as a  
67 tentative minimum age of 1,200 ka for the cave based solely on the age of the corals encrustation as  
68 provided by Antonioli et al. (2012; 2014)

69 Here we adopt a multidisciplinary and quantitative approach by combining geodetic measurements,  
70 dating techniques, geological and paleoecological observations and reconstructed RSL curves that are  
71 based on proxy data and numerical modelling. We aim at pinpointing the elevation of the uplifting  
72 stalactite in time and with respect to the fluctuating sea level. Our main goal is to correlate the marine  
73 ingressions that are observed within the stalactite section to the RSL changes that characterize the  
74 proxy-based sea-level curves. We evaluate the bathymetric conditions during the last flooding event  
75 with respect to present-day local sea level.

76

## 77 **2. Geological settings and Quaternary uplift rate**

78 NWS is a segment of the Early Miocene to present-day Sicilian-Maghrebian Fold and Thrust Belt (Fig.  
79 2). The latter consists of a thin-skinned, south-verging fold and thrust system formed by Mesozoic–  
80 Tertiary carbonates, siliciclastic and evaporites, locally overlain by late orogenic clastic deposits  
81 (Catalano et al., 2000). Quaternary extensional and strike-slip faults deformed the nappe pile and  
82 formed structural ridges and intervening basins (Mauz et al., 1997). Post Middle-Pleistocene coastal  
83 terraces are presently distributed around the NWS at elevations up to 160 m above modern mean sea  
84 level (msl) (Di Maggio et al., 2009), thus demonstrating that vertical uplift occurred as a consequence  
85 of deep-seated processes. A swarm of NW-SE and N-S/NNE-SSW trending faults accommodates the  
86 structural separation between the Rocca Rumena Ridge, where the cave karst formed, and the  
87 Castelluzzo and Cornino coastal plains (Fig. 2; Catalano et al., 2006). Close to Custonaci, eolian  
88 deposits (Fig. 3a and b) and shallow marine depositional systems (Fig. 3c and d) are preserved above  
89 Mesozoic-Paleogene carbonates at an elevation of  $120 \pm 10$  m above msl in close proximity to the RKC  
90 (see Fig. 2; Di Maggio et al., 2009). Although index fossils in these deposits are lacking, based on  
91 regional stratigraphic correlations, it has been proposed that they formed during the transgressive  
92 depositional cycle of the Early Pleistocene Calabrian Stage, which comprises the Marine isotope Stages  
93 (MIS) 53-35 (Ruggeri et al., 1979). The absolute age of  $1.48 (\pm 0.10)$  Ma inferred for the oldest  
94 deposits (Ruggeri et al., 1979) suggests a long-term linear uplift rate of  $0.081 \pm 0.014$  mm yr<sup>-1</sup>. The latter  
95 is consistent with a shorter-term estimate of  $\sim 0.08$  mm yr<sup>-1</sup> that is based on MIS 5e ( $\sim 125,000$  years  
96 ago and assuming an elevation of  $\sim 6.0$  m above msl paleo sea level) elevated coastal terraces that lie  
97 approximately 1 km to the west at  $\sim 16$  m above msl (Antonioli et al., 2002; Lambeck et al., 2004).

98

### 99 **3. Materials and Methods**

100 Here we describe our multidisciplinary approach that incorporates instrumental geodetic measurements  
101 of the stalactite elevation, laboratory analytical dating techniques for the age of speleothem and fossil  
102 corals and numerical modelling of RSL change.

103

### 104 **3.1 Orthometric height of the stalactite**

105 The orthometric height of the stalactite is the result of two integrated different geodetic surveying  
106 techniques: tacheometric and GNSS methods (Dardanelli et al., 2009). A static GNSS survey was  
107 conducted on several control points close to the RKC with the following acquisition parameters: 10 km  
108 baseline distance, observation time 4 hours for each point, cut-off angle 10 degrees and rate 5 seconds.  
109 The goal of the survey was the estimation of geoid undulation within the investigated zone. The data  
110 were calculated relative to the reference station TRAP (Trapani) of the UNIPA NRTK GNSS  
111 permanent GNSS network (Dardanelli et al., 2009); the geodetic undulation is approximately 43.52 m.  
112 A triple-difference analysis was performed by means of Network Deformation Analysis software  
113 package, which makes ionospheric and tropospheric corrections. The modelling of the tropospheric  
114 delay was carried out by using the ideal gas law refractivity model published by (Saastamoinen, 1972;  
115 Niell, 1996), while the modelling of ionospheric error was performed using the Total Electron Content  
116 (Klobuchar, 1996) with daily parameter values supplied by the Center for Orbit Determination in  
117 Europe of the Astronomical Observatory of the University of Bern. In addition, the ocean loading  
118 correction and the zenith troposphere delay estimation (which affects the baseline coordinates) were  
119 based on a hydrodynamic model (Schwidorski, 1980). We also performed a correction of antenna phase  
120 centre position using precise ephemeris. To fix the phase ambiguity, we used the LAMBDA method  
121 associated with a secondary test on the “ratio” (Teunissen et al., 1995), inserting the parameters of  
122 rotation of the Earth (Earth Orientation Parameters) and the values of the ocean tides to obtain an  
123 accurate result. The difference in elevation between the stalactite and the known points was derived by  
124 means of tacheometric levelling. Using the backward intersection method, we connected the  
125 tacheometric survey inside the cave to the GNSS survey.

126

### 127 **3.2 U/Th dating**

128 Two small pieces of carbonate (~ 200 mg) were extracted from the innermost and outermost layers of  
129 the stalactite (Fig. 1f) using a diamond-studded blade. The fragments were mechanically cleaned using  
130 the diamond blade to remove any visible contamination, leached with 0.1 HCl and dissolved with  
131 diluted HCl. The solution was equilibrated with a mixed  $^{236}\text{U}/^{233}\text{U}/^{229}\text{Th}$  spike, and the U and Th  
132 fractions were separated using UTEVA resin (Eichrom Technologies, USA). U and Th separation and  
133 purification followed a procedure slightly modified from Douville et al., (2010). Uranium and thorium  
134 isotopes were analysed using a ThermoScientific NeptunePlus MC-ICP-MS at the Laboratoire des  
135 Sciences du Climat et de l'Environnement in Gif-sur-Yvette. Mass bias was corrected using an  
136 exponential mass fractionation law (normalized to the natural  $^{238}\text{U}/^{235}\text{U}$  isotopic ratio) and the  
137 standard/sample bracketing technique (using a mixture of our triple spike and HU-1). For more details  
138 on the analytical procedure see Pons-Branchu et al. (2014).

139

### 140 **3.3 Strontium isotope analysis**

141 Numerical ages of the encrusted corals (Fig. 1f) were estimated using Sr isotopes measured at the  
142 Laboratoire des Sciences du Climat et de l'Environnement in Gif-sur-Yvette (France). Three small  
143 coral fragments (3-5 mg) corresponding to the thecal walls were extracted from the outermost coral  
144 overgrowth (Fig. 1f) and carefully cleaned using a handheld dental drill bit in order to remove the  
145 external bioeroded zone, corresponding to ~ 400  $\mu\text{m}$ . The internal portion was further polished upon  
146 removal of other visible contaminants. The sub-samples were examined using a binocular microscope  
147 to ensure against the presence of deep-penetrating and sediment-filled cavities and finally crushed into  
148 a powder with an agate mortar and pestle. The coral powder was rinsed three times with MilliQ water  
149 in acid-cleaned bullets before leaching with 0.3% acetic acid to remove 30-40% of  $\text{CaCO}_3$ . This first  
150 leaching step is designed to remove ions from exchangeable or leachable sites on the mineral surfaces.  
151 The remaining material was rinsed with MilliQ water and leached again with 0.4% acetic acid to  
152 remove 30% of the  $\text{CaCO}_3$  for analysis, following the procedure published by Li et al. (2011). The

153 supernatant solutions were evaporated and adjusted to 3N HNO<sub>3</sub> for ion exchange chromatography.  
154 The solutions were loaded into 300 µl columns containing 100-150 µm bead size Eichrom Sr-SPEC  
155 resin to remove matrix and isolate Sr from other major and trace elements (e.g., the interfering  
156 elements Ca, Rb and REE). The columns were pre-flushed with 1 ml 3N HNO<sub>3</sub> and 3 ml MilliQ-water  
157 and conditioned using 1 ml 3N HNO<sub>3</sub>. Strontium was eluted from the columns with 2.5 ml MilliQ-  
158 water, and each solution was adjusted to 0.5 N HNO<sub>3</sub> for isotopic measurements. A chemical blank was  
159 also prepared, following identical procedural steps. Strontium isotope ratios were measured using a  
160 multicollector-ICPMS ThermoScientific Neptune Plus. All the solutions were diluted to 50 ppb of Sr  
161 and introduced into the Neptune using an ESI-APEX desolvating system and a 100 µl/min nebulizer.  
162 The sensitivity of the 50 ppb Sr solution was approximately 8 V at the <sup>88</sup>Sr peak, and the chemical  
163 blank level was 0.008 V. The samples and standards were analysed in a static multi-collection mode in  
164 a single block of 50 cycles with an integration time of 8 seconds per cycle. The instrumental mass  
165 fractionation was corrected for by using a stable isotopic <sup>86</sup>Sr/<sup>88</sup>Sr ratio of 0.1194 and an exponential  
166 law. No isobaric corrections for Ca dimers and argides were required, and only minor corrections for  
167 <sup>87</sup>Rb to <sup>87</sup>Sr were considered. A correction was also applied for krypton isobaric interferences.  
168 Repeated measurements of strontium isotope standard NBS-987 during the analytical session yielded a  
169 mean <sup>87</sup>Sr/<sup>86</sup>Sr value of 0.710264 ± 0.000014 (2σ SD, n = 11, corresponding to an external  
170 reproducibility of 20 ppm). The <sup>87</sup>Sr/<sup>86</sup>Sr ratio for all the samples was corrected for instrumental bias to  
171 an accepted value for NBS-987 of 0.710248 (McArthur et al., 2001). All the <sup>87</sup>Sr/<sup>86</sup>Sr ratios were  
172 converted into numerical ages using the regression curves LOWESS look-up Table version 4: 08/04  
173 (revised from Li et al., 2011; see Table 1). The total uncertainty in <sup>87</sup>Sr/<sup>86</sup>Sr (±0.000014) was calculated  
174 by adding in quadrature the analytical uncertainty on the standard measurement (2σ SD = ±0.000014)  
175 to the uncertainty of the LOWESS curve for the period considered (0-2 Ma = ±0.000003), as suggested  
176 in equation 7.1 from McArthur et al., (2012). The lower and upper bounds on the ages were calculated  
177 based on the total <sup>87</sup>Sr/<sup>86</sup>Sr uncertainty (Table 1).

178

### 179 **3.4 Reconstructed RSL curves**

180 Three independent RSL change scenarios are considered for the time interval between 0.9 and 1.5 Ma.  
181 The RSL-ANICE scenario consists of an ensemble of RSL curves that are based on the ANICE global  
182 ice-sheet chronology (De Boer et al., 2014). The predicted RSL curves account for local Glacial  
183 Isostatic Adjustment (GIA) and result from the solution of the gravitationally self-consistent sea level  
184 equation (SLE; Farrell and Clark, 1976) for a suite of mantle viscosity profiles. We solve the SLE by  
185 means of the pseudo-spectral method (Mitrovica and Milne, 2003) with SELEN Fortran 90 code  
186 (Spada and Stocchi, 2007). The solid Earth response to ice-sheet fluctuations is accounted for by a  
187 spherical, self-gravitating, rotating, radially stratified, deformable but incompressible Maxwell  
188 viscoelastic Earth rheological model (Mitrovica and Milne, 2003; Spada and Stocchi, 2007). We keep  
189 the elastic lithosphere thickness fixed to 100 km. We vary the upper and lower mantle viscosity values  
190 between  $0.25$  to  $1.0 \times 10^{21}$  and  $2$  to  $10 \times 10^{21}$  Pa·s, respectively, and generate a combination of 20  
191 different mantle viscosity profiles. The second input of the SLE is the forcing function, which  
192 represents the continental ice-sheet fluctuations through time. We employ two versions of the 2.2  
193 million years long ice-sheet chronology that is described by ANICE ice-sheet model (De Boer et al.,  
194 2014). The first version does include the contribution of summer austral insolation (SAI) to the  
195 Antarctic Ice Sheet (AIS) variability (see AIS-SAI in Fig. 4), while in the second version of ANICE the  
196 SAI is not accounted for (see AIS-NSAI in Fig. 4). Including SAI results in significant retreats of AIS  
197 during the interglacials that characterize the MPT (Fig. 4). We solve the SLE for 40 models (20  
198 viscosity profiles x 2 ANICE versions) and compute the RSL curves at the location of the speleothem  
199 (red curve in Fig. 5a). The second RSL scenario (RSL-Rohling14) is based on the RSL curve for  
200 Gibraltar that was derived by Rohling et al. (2014) through statistical analysis of previously published  
201 proxy data from Wang et al. (2010; green curve in Fig. 5a). The third scenario (RSL-Elderfield12) is  
202 complementary to RSL-Rohling14 and is based on proxy data from Elderfield et al. (2012; green curve

203 in Fig. 5a). Both proxy-based curves are corrected for the differential GIA response.  
204 The average RSL change in time and its standard deviation are evaluated for all three RSL scenarios.  
205 These values are then used to randomly generate, by means of a Monte Carlo method, a normal  
206 distribution of RSL values in time. The same is done for the reconstructed elevation of the speleothem  
207 (based on linear interpolation). The four normal distributions are then overlaid to evaluate the  
208 probability (in time) for the speleothem to be intercepted by sea level and, consequently, to be located  
209 at a certain depth with respect to sea level.

210

#### 211 **4. Results**

212 On the basis of the method described in Section 3.1, we estimate the orthometric height of the stalactite  
213 to be 97.12 m. By shifting the current elevation of the speleothem back in time according to the linear  
214 uplift rate of  $0.081 \pm 0.014 \text{ mm yr}^{-1}$  (see Section 2) and assuming that sea level has remained constant  
215 through time, an interception with current msl occurs at  $\sim 1.225 \text{ Ma}$  (Fig. 5a). Both calculated U/Th  
216 ages for the spelean carbonate layers are beyond the upper limit of the  $^{230}\text{Th}$  age range, indicating an  
217 age older than  $\sim 0.6 \text{ Ma}$  (Cheng et al., 2013). The age of the stalactite is indirectly determined by  
218 analysing the coral overgrowth using the strontium isotope dating method (see Section 3.3). The  
219  $^{87}\text{Sr}/^{86}\text{Sr}$ -derived ages of the three coral fragments encrusting the external surface of the speleothem are  
220 identical within error (Table 1), suggesting that the coral portions, which were carefully selected from  
221 the internal part of the thecal walls, were most likely pristine, and the ages can be considered reliable.  
222 Averaging the values of the three fragments yields a mean age for the corals of  $1.124 \pm 0.2 \text{ Ma}$ , which  
223 represents the age of the last marine ingression. The calculated standard deviation corresponds to  $2\sigma$   
224 SD of the mean age. The latter broadly agrees with the age of interception between the speleothem and  
225 current msl.

226 The predicted RSL-ANICE ensemble is characterized by lower amplitude RSL fluctuations with  
227 respect to the proxy-based scenarios (Fig. 5a). In particular, the predicted RSL highstands during the

228 interglacial periods are significantly lower. Maximum RSL elevations of 4-6 m above current msl are  
229 found for MIS 25, 31 and 37 and only for GIA solutions that account for the combination of the AIS  
230 sensitivity to austral summer insolation (see AIS-SAI in Fig. 4) and a high viscosity contrast between  
231 the upper and lower mantle.

232 When the three RSL scenarios are adopted, different numbers and timings of intersections between the  
233 uplifting stalactite and sea level occur at different elevations above current msl (Fig. 5a). The age and  
234 elevation of old shallow marine deposits, together with the age of the coral overgrowth and the number  
235 of hiatuses within the stalactite, are necessary constraints to reconstruct the chronology of marine  
236 inundations. In particular, the permissible living depth range for the corals is fundamental to pinpoint  
237 the elevation of the stalactite with respect to sea level during the fourth marine ingressions. Of the coral  
238 species that have been identified, *Cladopsammia rolandi* indicates a water depth  $\geq 20$  m, with  
239 specimens capable of surviving at depths  $\geq 50$  m under normal light conditions (Rosso et al., 2015;  
240 Zibrowius, 1978). A water column height of 20 m above the stalactite is assumed as the minimum limit  
241 for the RSL peak height during the formation of the coral. Accordingly, we use a Monte Carlo  
242 approach to generate normal distributions around the mean values of, respectively, the elevation of the  
243 stalactite through time and the three RSL scenarios (Fig. 5a). We evaluate the probability in time that  
244 the reconstructed RSL was at least 20 m above the predicted elevation of the cave within the plausible  
245 age range for the formation of the coral. We find that the RSL-ANICE ensemble is able to satisfy the  
246 minimum depth requirement during the fourth marine ingressions with very low probabilities,  $\sim 15\%$  and  
247  $\sim 10\%$  for MIS 37 and 41, respectively (see Fig. 5b). Solutions for RSL-Rohling14 indicate MIS 37 and  
248 35 as the most likely events, with probabilities of 65% and 35%, respectively (see Fig. 5b). The same  
249 occurs for RSL-Elderfield12 scenarios, with the largest probability (100%) achieved for MIS 37,  
250 followed by MIS 35 (85%), MIS 39 (60%) and MIS 41 (65%) (see Fig. 5b).

251

252 **5. Discussion**

253 The requirement of a maximum of three interceptions before the formation of the coral encrustation  
254 restricts the range of plausible solutions and shifts the chronological sequence of events to before the  
255 MIS 31 interglacial. Although MIS 37 is the most likely event for each of the three scenarios (Fig. 5b),  
256 the occurrence of a comparable RSL peak immediately afterwards suggests that the formation of the  
257 corals occurred during MIS 35, which is also closer in time to the mean age of the corals. The RSL  
258 highstands that follow MIS 35 are characterized by lower amplitudes. According to the RSL-Rohling14  
259 and RSL-Elderfield12 scenarios, two interceptions between the stalactite and sea level might have  
260 occurred after MIS 35 and before MIS 23. However, these would have resulted in lower highstands that  
261 could not have interfered with previous coral encrustations. After MIS 25 the transition towards non-  
262 linear responses of ice sheet to astronomical and climatological parameters resulted in long-period  
263 glaciations that, together with the uplift, prevented further marine inundation of the RKC.

264 The local sea level during the MIS 35 interglacial was 20-30 m higher than present, which suggests that  
265 a significant retreat of the West and East Antarctic Ice Sheet (WAIS and EAIS, respectively) occurred.  
266 The ANICE ice-sheet model reconstruction does not show a significant retreat of the AIS because the  
267 ice-sheet reconstruction is largely driven by the smoothed  $\delta^{18}\text{O}$  stack curve (Lisiecki and Raymo,  
268 2005), whereas regional RSL records might show more amplified variability (De Boer et al., 2014;  
269 Konijnendijk et al., 2016). A marine transgression during MIS 35 was reported in form of a change in  
270 mollusks species recorded by sediments in the slowly uplifting northern Po Plain (Gianolla et al.,  
271 2010). This correlates to an RSL highstand that was observed for the same region by Scardia et al.  
272 (2006). Deep-sea sediment cores from two drilling sites off East Antarctica (Prydz Bay and South  
273 Atlantic), however, show that ice-rafted debris was still being produced during MIS 35 (Teitler et al.,  
274 2015). This implies that there was an active sector of the EAIS that was capable of launching icebergs  
275 into the Southern Ocean. Only later, between MIS 33 and 31, did a widespread retreat of AIS, with  
276 increased contributions from EAIS, occur, resulting in an abrupt change in sedimentation. We argue,  
277 therefore, that the drilling sites studied by Teitler et al. (2016) might have been mostly sensitive to the

278 northeastern portion only of the EAIS, which was still active during the MIS 35 interglacial. The far-  
279 field site of Custonaci, instead, recorded the cumulative response of local sea level to the retreat of  
280 WAIS and southern portions of EAIS.

281

## 282 **6. Conclusions**

283 The RKC speleothem section is the oldest stalactite containing marine hiatuses ever studied to date and  
284 is the first direct geological evidence of RSL changes during the MPT. The formation and subsequent  
285 preservation of the three hiatuses and of the corals encrustation are direct consequences of two  
286 independent processes that worked in opposite direction. Quaternary uplift, which is a reflection of  
287 deep-seated geodynamic processes, first facilitated marine incursions by elevating the RKC towards  
288 msl. During this time, higher-frequency RSL fluctuations left permanent marks in the speleothem,  
289 which was very close to current msl. The transition from 41,000 to 100,000 periodicity in RSL  
290 fluctuations contributed to the permanent disconnection of the uplifting cave with msl and prevented  
291 any further inundation. The corals encrustations, which mark the last marine incursion, show that local  
292 sea level rose up to 20-30 m above present. This implies that among the several factors that contributed  
293 to local RSL rise, a significant AIS retreat likely occurred. Our results, combined with coeval AIS-  
294 proximal sedimentological observations, confirm that the variability of AIS during climate transitions  
295 is sectoral (Teitler et al., 2015). The evidence presented in this study agrees with predictions for both  
296 the past and near future of AIS response to climate variability and show that different portions of EAIS  
297 likely contribute to sea-level highstands during warm periods (Pollard and De Conto, 2009; Dutton et  
298 al., 2015).

299

300

301

302

303

304 **References and Notes:**

305 Antonioli, F., Cremona, G., Immordino, F., Puglisi, C., Romagnoli, C., Silenzi, S., Valpreda, E., and  
306 Verrubbi, V., 2002, New data on the Holocene sea-level rise in NW Sicily (Central  
307 Mediterranean Sea): *Global and Planetary Change*, v. 34, p. 121-140.

308 Antonioli, F., Montagna, P., Caruso, A., Ruggieri, R., Lo Presti, V., Silenzi, S., Frank, N., Douville, E.  
309 and C. Pierre, 2012, Investigation of marine and continental layers in a stalactite older than 1  
310 million years (Custonaci, north-western sector of Sicily), *SLALOM 2012*, abstract volume,  
311 Athens 19–22 March 2012, p. 57–58.

312 Antonioli, F., Ruggieri, R., Montagna, P., Pepe, F., Caruso, A., Stocchi, P., Renda, P., Lo Presti, V.,  
313 Frank, N., Douville, E., Pierre, C., Messina Panfalone, D., 2014, The geosite Rumena cave a  
314 unique paleoclimate and sea level archive in the Mediterranean area (northwestern Sicily). 4<sup>th</sup>  
315 International Symposium, Karst Geosites, abstract volume, Favignana 30 May – 2 June, p. 64–  
316 66.

317 Antonioli, F., Lo Presti, V., Rovere, A., Ferranti, L., Anzidei, M., Furlani, S., Mastronuzzi, G., Orru,  
318 P.E., Scicchitano, G., and Sannino, G., 2015. Tidal Notches in Mediterranean Sea: a  
319 comprehensive analysis. *Quaternary Science Reviews*, 119, 66-84.

320 Artyushkov, E.V., 2012, Vertical crustal movements on the continents as a reflection of deep-seated  
321 processes in the earth's crust and mantle: Geological effects. *Herald of the Russian Academy of*  
322 *Sciences*, v. 82, no. 6, p. 432-446.

323 Bintanja, R., Van de Wal, R.S.W., and Oerlemans, J., 2005, Modelled atmospheric temperatures and  
324 global sea level over the past million years: *Nature*, v. 437, p. 125-128.

325 Breitenbach, S., Fernandez, D., Adkins, J., Mingram, B., Oberhänsli, H., and Haug, G., 2005,  
326 Speleothem records older than 500 ka from Southern Siberia: *Proc. 14th International*

327 Conference of Speleology, Athens 2005, p. 1-7.

328 Catalano, R., Franchino, A., Merlino, S., and Sulli, A., 2000, Central western Sicily structural  
329 setting interpreted from seismic reflection profiles: *Mem. Soc. Geol. It.*, v. 55, p. 5-16.

330 Catalano, R., Abate, B., Agate, M., Basilone, L., Di Maggio, C., Di Maio, D., Mancuso, M.,  
331 Sulli, A., Vaccaro, F., Arnone, M., Avellone, G., Barchi, M., Bonomo, S., Cottone, S.,  
332 D'Argenio, A., Fallo, L., Lo Cicero, G., Lo Iacono, C., Lucido, M., Pepe, F., Scannavino, M.,  
333 and Sprovieri, R., 2006, Carta geologica d'Italia alla scala 1:50.000 del foglio 593  
334 "Castellammare del Golfo": Progetto CARG, p. 1.

335 Cheng, H., Edwards, R.L., Shen, C.-C., Polyak, V.J., Asmeron, Y., Woodhead, J., Hellstrom, J., Wang,  
336 Y., Kong, X., Spötl, C., Wang, X., Alexander Jr., E.C., 2013, Improvements in  $^{230}\text{Th}$  dating,  
337  $^{230}\text{Th}$  and  $^{234}\text{U}$  half-life values, and U/Th isotopic measurements by multi-collector inductively  
338 coupled plasma mass spectrometry. *Earth and Planetary Science Letters*, v. 371-372, p. 82–91.

339 Clark, P.U., and Pollard, D., 1998, Origin of the middle Pleistocene transition by ice sheet erosion of  
340 regolith: *Paleoceanography*, v. 13, no. 1, p. 1-9.

341 Dardanelli, G., Franco, V., Lo Brutto, M., 2009, Accuracy and reliability in GNSS NRTK, Proceedings  
342 of European Navigation Conference - Global Navigation Satellite Systems, Naples, Italy.

343 De Boer, B., Van de Wal, R.S.W., Lourens, L.J., and Bintanja, R., 2013, A continuous simulation of  
344 global ice volume over the past 1 million years with 3-D ice-sheet models: *Climate Dynamics*,  
345 v. 41, p. 1365-1384.

346 De Boer, B., Lourens, L.J., and Van de Wal, R.S.W., 2014, Persistent 400,000-year variability of  
347 Antarctic ice volume and the carbon cycle is revealed throughout the Plio-Pleistocene: *Nature*  
348 *Communications*, v. 5:2999, doi:10.1038/ncomms3999.

349 Di Maggio, C., Agate, M., Contino, A., Basilone, L., Catalano, R., 2009. Unconformity-bounded  
350 stratigraphic units of Quaternary deposits mapped for the CARG Project in Northern and  
351 Western Sicily: *Alpine and Mediterranean Quaternary*, v. 22, 2, 354-364.

352 Douville E., Salle E., Frank N., Eisele M., Pons-Branchu E., Ayrault S., 2010, Rapid and accurate U-  
353 Th dating of ancient carbonates using inductively coupled plasma-quadrupole mass  
354 spectrometry: *Chemical Geology* 272, 1-11.

355 Dutton A., Antonioli F., Bard E., M. Esat T., Lambeck K, McCulloch M., 2009. Phasing and amplitude  
356 of sea level and climate change during the penultimate interglacial. *Nature Geosciences*, 355-  
357 359.

358 Dutton, A., Carlson, A.E., Long, A.J., Milne, G.A., Clark, P.U., DeConto, R., Horton, B.P., Rahmstorf,  
359 S., and Raymo, M.E., 2015. Sea-level rise due to polar ice-sheet mass loss during past warm  
360 periods. *Science*, v. 349, doi:10.1126/science.aaa4019.

361 Elderfield, H. et al., 2012, Evolution of ocean temperature and ice volume through the Mid-Pleistocene  
362 Climate Transition. *Science* 337, 704–709.

363 Farrell, W.E., and Clark, J.A., 1976, On postglacial sea level: *Geophys. J.R. Astron. Soc.*, v. 46, p.  
364 647-667.

365 Ferranti, L., Antonioli, F., Mauz, B., Amorosi, A., Dai Pra, G., Mastronuzzi, G., Monaco, C., Orrù, P.,  
366 Pappalardo, M., Radtke, U., Renda, P., Romano, P., Sansò, P., Verrubbi, V., 2006. Markers of  
367 the last interglacial sea-level high stand along the coast of Italy: tectonic implications.  
368 *Quaternary International* 145-146, 30–54.

369 Gianolla, D., Negri, M., Basso, D., and Sciunnach, D., 2010. Malacological response to Pleistocene  
370 sea-level change in the northern Po Plain, N. Italy: detailed palaeoenvironmental  
371 reconstructions from two lombardian cores. *Rivista Italiana di Paleontologia e Stratigrafia*, vol.  
372 116, no. 1, pp. 79-102.

373 Grant, K.M., Rohling, E.J., Bronk Ramsey, C., Cheng, H., Edwards, R.L., Florindo, F., Heslop, D.,  
374 Marra, F., Roberts, A.P., Tamisiea, M.E., & Williams, F., 2014, Sea-level variability overt  
375 five glacial cycles: *Nature Communications*, doi:10.1038/ncomms6076.

376 Klobuchar, J. A., 1996, *Global Positioning System: Theory and Applications*. Volume I, Cap. XII:

377 Ionospheric effects on GPS, pp. 485-515, American Institute of Aeronautics and Astronautics  
378 Inc.

379 Konijnendijk, T.Y.M., Ziegler, M., and Lourens, L.J., 2016. On the timing and forcing mechanisms of  
380 late Pleistocene glacial terminations: Insights from a new high-resolution benthic stable oxygen  
381 isotope record of the eastern Mediterranean, *Quaternary Science Reviews*, 129, 308-320, doi:  
382 10.1016/j.quascirev.2015.10.005.

383 Kopp, R.E., Simons, F.J., Mitrovica, J.X., Maloof, A.C., and Oppenheimer, M., 2009, Probabilistic  
384 assessment of sea level during the last interglacial stage: *Nature*, v. 462, p. 863-868.

385 Lambeck, K., Antonioli, F., Purcell, A., and Silenzi. S., 2004, Sea level change along the Italian coast  
386 for the past 10,000 years: *Quaternary Science Reviews*, v. 23, p. 1567-1598.

387 Li D., Shields-Zhou G.A., Ling H.F., Thirlwall M. (2011). Dissolution methods for strontium isotope  
388 stratigraphy: Guidelines for the use of bulk carbonate and phosphorite rocks. *Chemical Geology*  
389 290, 133-144.

390 Lisiecki, L., and Raymo, M., 2005, A Pliocene-Pleistocene stack of 57 globally distributed benthic  
391  $\delta^{18}\text{O}$  records: *Paleoceanography*, v. 20, PA1003, doi:10.1029/2004PA001071.

392 Mauz, B., Buccheri, G., Zoller L., and Greco, A., 1997, Middle to upper Pleistocene morphostructural  
393 evolution of the NW coast of Sicily: thermoluminescence dating and paleontological  
394 stratigraphical evaluations of littoral deposits: *Palaeogeogr. Palaeoecol. Palaeogeogr.*, v. 128, p.  
395 269-285.

396 McArthur J.M., Howarth R.J. and Bailey T.R. (2001) Strontium Isotope Stratigraphy: LOWESS  
397 Version 3: Best Fit to the Marine Sr-Isotope Curve for 0–509 Ma and Accompanying Look-up  
398 Table for Deriving Numerical Age, *The Journal of Geology*, 109, 155–170.

399 McArthur J.M., Howarth R.J. and Shields G.A. (2012) Strontium Isotope Stratigraphy. In Gradstein F.,  
400 Ogg. J., Schmitz M. and Ogg G. (Eds), *The Geologic Time Scale 2012*, ed. Elsevier, 127-144.

401 Mitrovica, J.X., and Milne, G.A., 2003, On post-glacial sea level: I. General theory. *Geophys. J. Int.*, v.

402 154, p. 253-267.

403 Niell, A. E, 1996, Global mapping functions for the atmosphere delay at radio wavelengths. *Journal of*  
404 *Geophysical Research*, vol. 100, n. B2:3227-3246.

405 Pollard, D. and Deconto, R.M., 2009. Modelling West Antarctic ice sheet growth and collapse through  
406 the past five million years. *Nature*, v. 458, p. 329-333.

407 Pons-Branchu E., Douville E., Roy-Barman M., Dumont E., Branchu P., Thil F., Frank N., Bordier L.,  
408 Borst W. (2014) A geochemical perspective on Parisian urban history based on U-Th dating,  
409 laminae counting and yttrium and REE concentrations of recent carbonates in underground  
410 aqueducts. *Quaternary Geochronology* 24, 44-53.

411 Richards D.A., Smart P.L., Edwards R.L., 1994, Maximum sea levels for the last glacial period from  
412 U-series ages of submerged speleothems, *Nature* 367, 357-360.

413 Rohling, E.J., Foster, G.L., Grant, K.M., Marino, G., Roberts, A.P., Tamisiea, M.E., and Williams, F.,  
414 2014, Sea-level and deep-sea-temperature variability over the past 5.3 million years: *Nature*, v.  
415 508, p. 477-482, doi:10.1038/nature13230.

416 Rovere, A., Raymo, M.E., Mitrovica, J.X., Hearthy, P.J., O’Leary, M.J., and Inglis, J.D., 2014. The  
417 Mid-Pliocene sea-level conundrum: Glacial isostasy, eustasy and dynamic topography. *Earth*  
418 *and Planetary Science Letters*, 387, 27-33.

419 Rosso, A., Sanfilippo, R., Ruggieri, R., Maniscalco, R., and Vertino, A., 2015, Exceptional record of  
420 submarine cave communities from the Pleistocene of Sicily (Italy): *Lethaia*, v. 48, p. 133-144.

421 Ruggieri, G., Sprovieri, R., and Unti M., 1979, Evidenze della trasgressione dell’Emiliano (Pleistocene  
422 inferiore) nella Sicilia Orientale: *Boll. Soc. Geol. It.*, v. 98, p. 469-473.

423 Ruggieri, R., and De Waele, J., 2014. Lower- to Middle Pleistocene flank margin caves at Custonaci  
424 (Trapani, NW Sicily) and their relation with past sea levels. *Acta Carsologica*, 43/1, 11–22.

425 Saastamoinen, J., 1972, Atmospheric correction for the troposphere and stratosphere in radio ranging of  
426 satellites, *Geophys. Monogr.*, 15, American Geophysical Union, Washington DC.

- 427 Scardia, G., Muttoni, G., and Sciunnach, D., 2006, Subsurface magnetostratigraphy of Pleistocene  
428 sediments from the Po Plain (Italy): Constraints on rates of sedimentation and rock uplift. *GSA*  
429 *Bulletin*, v. 118; no. 11/12; p. 1299–1312; doi: 10.1130/B25869.1.
- 430 Schwiderski, E. W., 1980, On charting global ocean tides, *Reviews of Geophysics and Space Physics*,  
431 18, 243-268.
- 432 Spada, G., and Stocchi, P., 2007, SELEN: A Fortran 90 program for solving the "sea-level equation":  
433 *Computers & Geosciences*, v. 33, p. 538-562.
- 434 Teitler, L., Florindo, F., Warnke, D.A., Filippelli, G.M., Kupp, G., and Taylor, B., 2015, Antarctic Ice  
435 Sheet response to a long warm interval across Marine Isotope Stage 31: A cross-latitudinal  
436 study of iceberg-rafted debris: *Earth and Planetary Science Letters*, v. 409, p. 109-119.
- 437 Teunissen, P. J. G., de Longe, P. J., Tiberius, C. C. J. M., 1995, The LAMBDA-method for fast GPS  
438 surveying. In: *International Symposium "GPS Technology Applications" Bucharest, Romania*.
- 439 Wang, P., Tian, J., and Lourens, L. J., 2010, Obscuring of long eccentricity cyclicity in Pleistocene  
440 oceanic carbon isotope records. *Earth Planet. Sci. Lett.* 290, 319–330.
- 441 Zibrowius, H., 1978, Les Scleractiniaires des grotte sous-marine en Mediterranee et dans l'Atlantique  
442 nord-orientale (Portugal, Madere, Canaries, Azores). *Pubblicazioni della Stazione Zoologica di*  
443 *Napoli* 40, 516 545.25.

444

445

446 **Acknowledgments:** We are thankful to David Richards, Christian Ohneiser and Enrico Di Stefano for  
447 their helpful comments. This work was partly financially supported by the grant "Fondo Finalizzato  
448 alla Ricerca 2012/2013 (CUP B71J12001450001)" funded by the University of Palermo (Italy).

449

450

451

452

453

454

455

456 **FIGURE CAPTIONS**

457 **Figure 1.** Study area (a) and details of the RKC (b-d). The cave wall (e) and the stalactite are covered  
458 by a coral encrustation. The stalactite section (f) reveals three concentric hiatuses. Lithophaga-  
459 produced boring holes penetrate the third hiatus. The external surface of the stalactite is covered by  
460 coral encrustations. The geographical coordinates of the RKC are 38.07 N and 12.66 E (UTM  
461 WGS84).

462

463 **Figure 2.** Simplified geological map of the study area in the North West Sicily (map adapted from the  
464 1:50.000 Geological Map at a scale 1:50.000 (CARG Project; Catalano et al., 2006).

465

466 **Figure 3.** Thin Sections A and B – (samples Cu 13.1 and Cu 13.4) Photos of the eolian sandstones (qz -  
467 quartz; IO - iron oxide). C and D – (samples Cu 13.10a and Cu 13.10b.) Photos of calcarenites rich in  
468 foraminifera (El, Elphidium sp.; Gr – Globigerinoides ruber; Ec – Echinoid spine). Sites samples are  
469 indicated in Fig. S1.

470

471 **Figure 4.** Antarctic Ice Sheet (AIS) and Greenland Ice Sheet (GIS) ice volumes (expressed in meters of  
472 eustatic sea-level change) according to ANICE (22). Neglecting SAI results in a larger-than-today AIS  
473 during the interglacials that punctuate the MPT (solid red curve, AIS-NSAI). Accounting for SAI,  
474 instead, triggers significant retreats that result in eustatic sea-level highstands above present-day msl  
475 (AIS-SAI; ~5.5 m at MIS 31, ~4 m at MIS 25, ~2m at MIS 37). For both scenarios, the GIS is slightly  
476 larger than today (~ 1 m esl) and is also quite stable throughout the period under considerations.

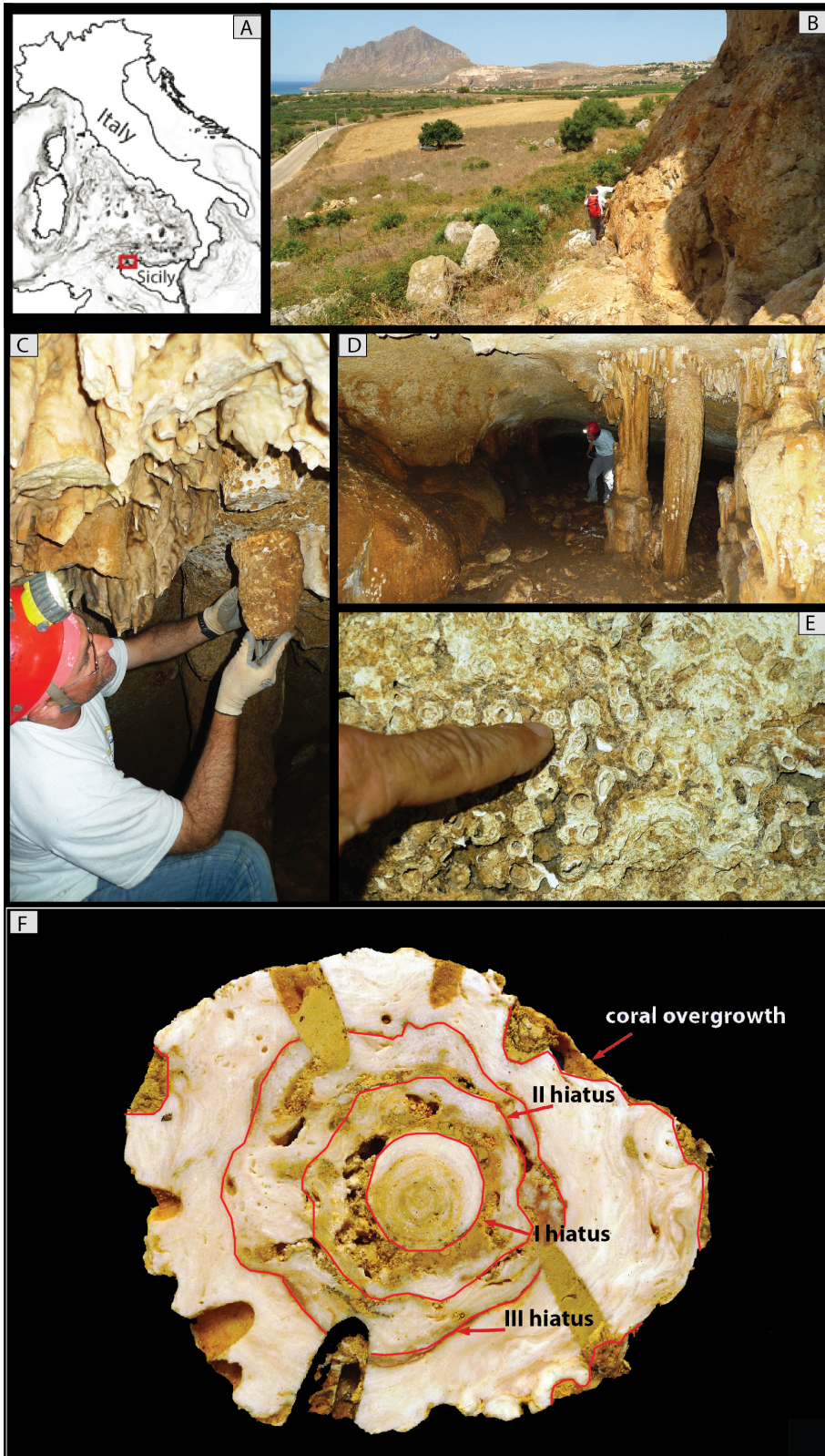
477

478 **Figure 5.** (a) Elevation of the RKC in time (mean and standard deviation; dotted blue lines) with  
479 respect to three rsl change scenarios (95% confidence interval): RSL-ANICE (red shading), RSL-  
480 Rohling14 (blue shading), RSL-Elderfield12 (grey shading). The horizontal double-headed arrow  
481 indicates the age interval for the formation of the coral encrustation. (b) Probability of a water column  
482 height  $\geq 20$  m above the corals according to the three rsl change scenarios. The probability decreases  
483 with time as a consequence of the uplift of the RKC and long-term rsl drop (with decreasing amplitude  
484 of shorter-term fluctuations).

485

486  
487  
488

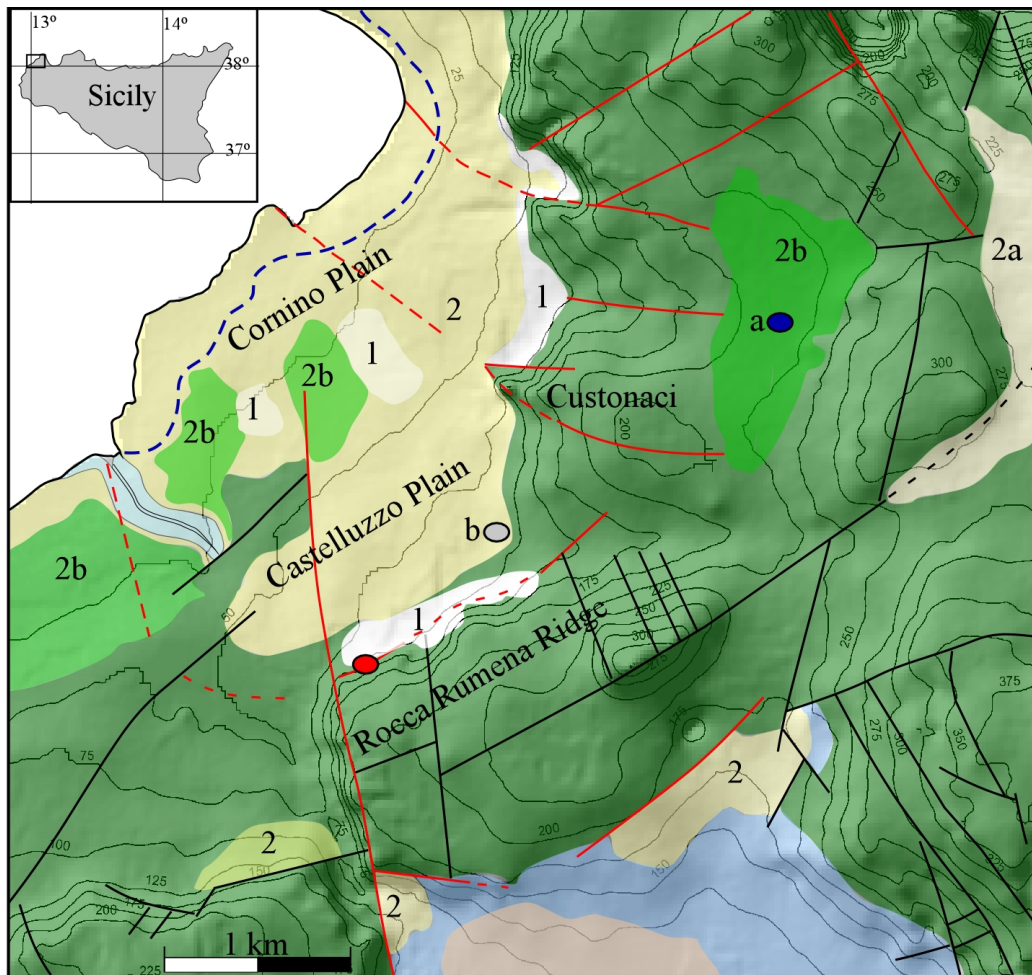
Figure 1



489  
490  
491

492  
493  
494  
495  
496

Figure 2



● Rumena karst cave    - - - Last Interglacial inner margin    / Strike-slip fault    / fault

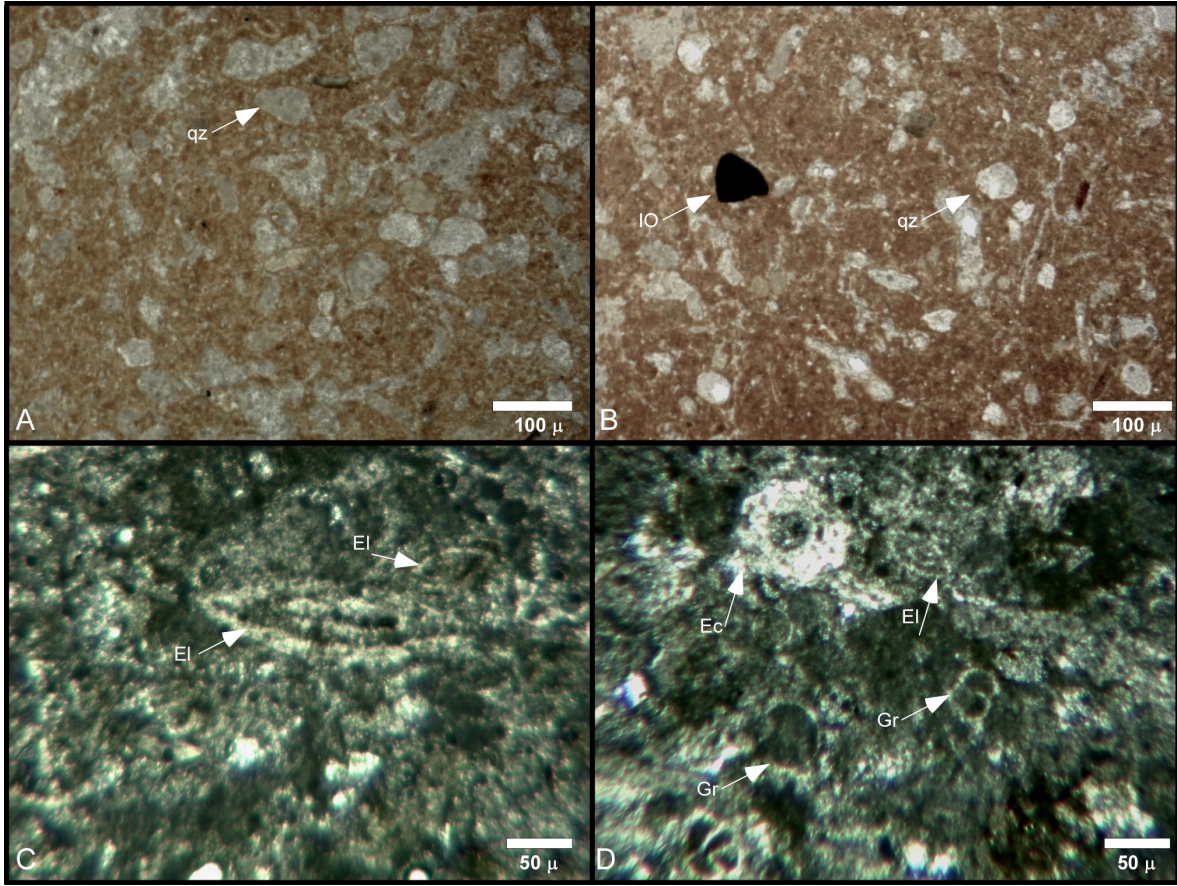
Sites samples    a ● Aeolian sandstones (A and B in Fig. S2)  
                              b ○ Calcarenites rich in foraminifera (C and D in Fig. S2)

1	Debris		Biocalcarenites, biocalcirudites with fragments of lamellibranches, clays with intercalated sand and sandstone layers with local lens of sand quartz and conglomerates. Early Miocene-middle Tortonian
2a	Bioclastic calcarenites and conglomerates (2), silt sand and gravel (2a), aeolian quartz-sand, paleosoils and colluvium (2b). Early Pleistocene	2b	Mesozoic-Paleogene carbonates
2			
	Clays, sands, sandstones, quartzarenites and conglomerates. Terravecchia Formation. Late Tortonian-Early Messinian		

497  
498  
499  
500  
501  
502

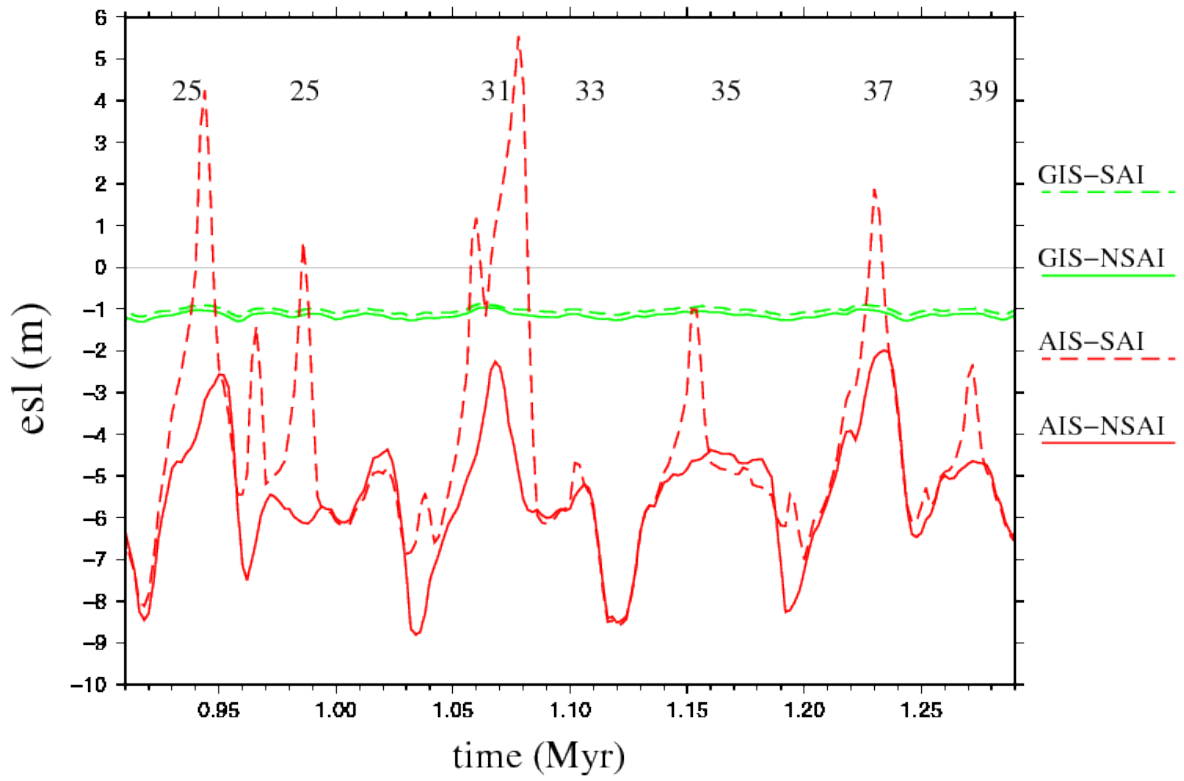
503  
504  
505  
506

**Figure 3**



507  
508  
509  
510  
511  
512  
513  
514  
515  
516  
517  
518  
519  
520  
521  
522  
523  
524  
525  
526  
527  
528

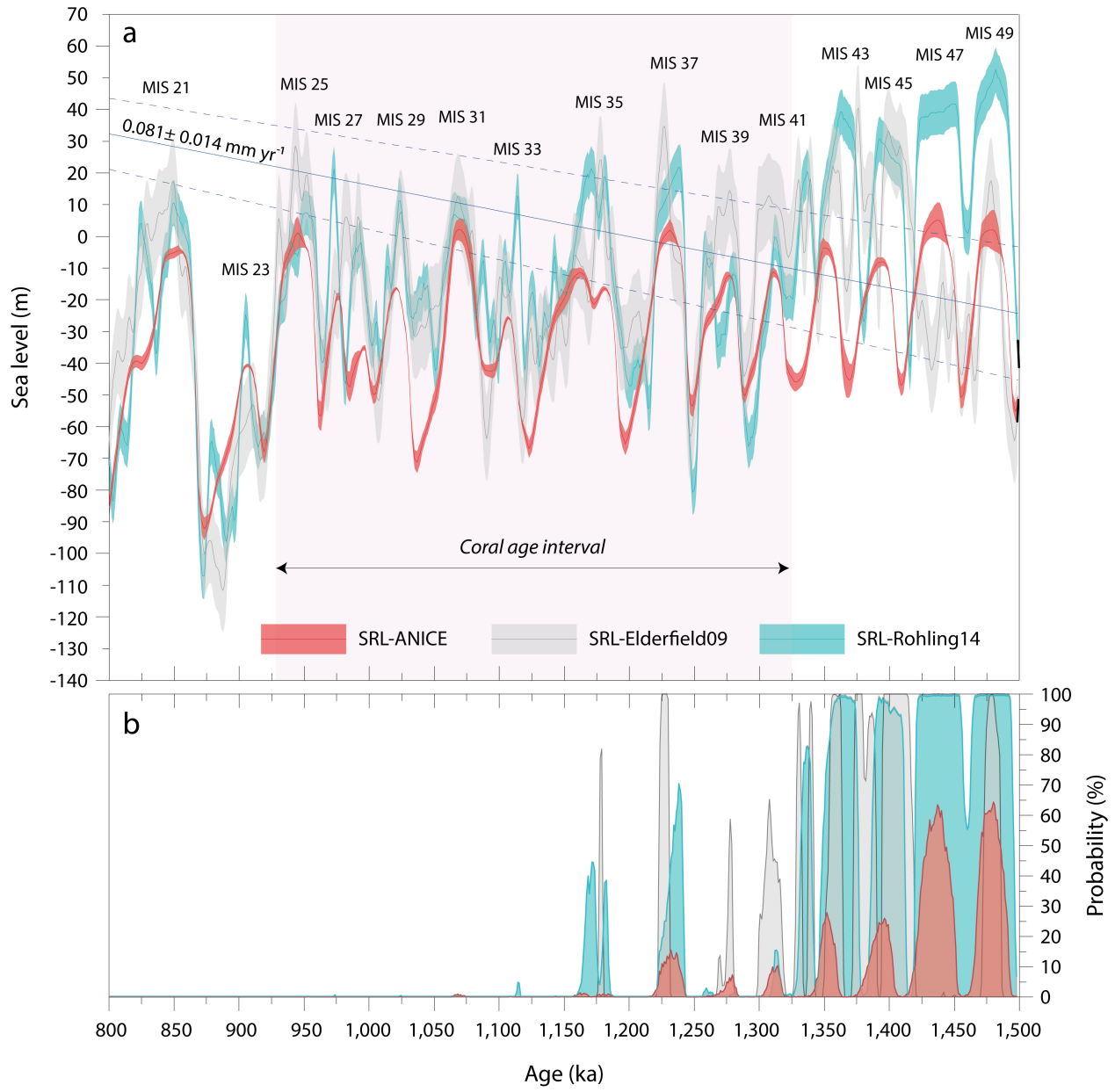
529 **Figure 4**  
530  
531



532  
533  
534  
535  
536  
537  
538  
539  
540  
541  
542  
543  
544  
545  
546  
547  
548  
549  
550  
551  
552  
553  
554

555  
556  
557  
558  
559

Figure 5



560  
561  
562  
563  
564  
565  
566  
567

568  
569  
570  
571  
572  
573

**TABLES**

574 **Table 1.**  $^{87}\text{Sr}/^{86}\text{Sr}$  ages (Ma) of the corals encrusting the stalactite.

<b>Sample ID</b>	<b>Material</b>	<b>Method</b>	<b><math>^{87}\text{Sr}/^{86}\text{Sr}</math></b>	<b>Lower Age (Ma)</b>	<b>Mean Age (Ma)</b>	<b>Upper Age (Ma)</b>
-2572-	Coral	MC-ICP-MS	0.709130 (14)	0.814	1.131	1.288
-2573-	Coral	MC-ICP-MS	0.709137 (14)	0.665	1.023	1.268
-2574-	Coral	MC-ICP-MS	0.709124 (14)	0.957	1.218	1.460
<b>Mean value</b>					<b>1.124</b>	
<b>2 SD</b>					<b>0.2</b>	

575